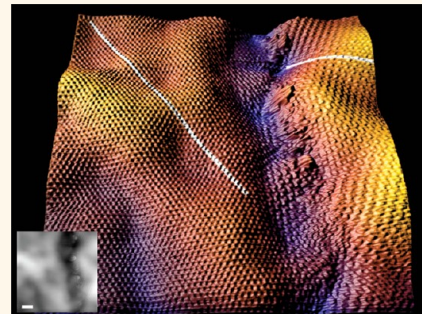


Atomic-Scale Evidence for Potential Barriers and Strong Carrier Scattering at Graphene Grain Boundaries: A Scanning Tunneling Microscopy Study

Justin C. Koepke,^{†,‡,*} Joshua D. Wood,^{†,‡,§} David Estrada,^{†,§} Zhun-Yong Ong,^{§,⊥} Kevin T. He,^{†,‡} Eric Pop,^{†,‡,§} and Joseph W. Lyding^{†,‡,§,*}

[†]Department of Electrical & Computer Engineering, [‡]Beckman Institute for Advanced Science and Technology, [§]Micro & Nanotechnology Lab, and [⊥]Department of Physics, University of Illinois, Urbana—Champaign, Illinois 61801, United States

ABSTRACT We use scanning tunneling microscopy and spectroscopy to examine the electronic nature of grain boundaries (GBs) in polycrystalline graphene grown by chemical vapor deposition (CVD) on Cu foil and transferred to SiO₂ substrates. We find no preferential orientation angle between grains, and the GBs are continuous across graphene wrinkles and SiO₂ topography. Scanning tunneling spectroscopy shows enhanced empty states tunneling conductance for most of the GBs and a shift toward more n-type behavior compared to the bulk of the graphene. We also observe standing wave patterns adjacent to GBs propagating in a zigzag direction with a decay length of ~1 nm. Fourier analysis of these patterns indicates that backscattering and intervalley scattering are the dominant mechanisms responsible for the mobility reduction in the presence of GBs in CVD-grown graphene.



KEYWORDS: graphene · CVD · grain boundaries · scanning tunneling microscopy · spectroscopy · scattering

Graphene is a two-dimensional, zero band gap semimetal with exceptional electrical properties.¹ Wafer-scale growth of monocrystalline graphene with a controllable number of layers is a primary challenge to integrating graphene into nanoelectronic devices and circuits which exploit these properties. Therefore, many researchers are investigating large-scale graphene synthesis by thermal decomposition of Si from SiC(0001)² surfaces and transfer to other substrates,³ as well as by chemical vapor deposition (CVD) on noble and transition metal substrates.^{4–8} Among these, CVD growth of graphene on Cu is interesting due to the ability to grow predominantly monolayer graphene⁶ and transfer it to other substrates. Since graphene growth on Cu is not epitaxial, this process leads to the formation of randomly oriented grains with shapes based on hydrogen etching, carbon diffusion, and other growth conditions.^{9–13} When these individual graphene grains coalesce into a film, graphene grain boundaries (GBs) form.

Recent theoretical studies of GBs^{14–16} predict modified electronic structures and transport barriers at certain periodic boundaries. Transmission electron microscopy (TEM) and atomic force microscopy (AFM) studies of graphene GBs show that the resulting GBs are aperiodic^{17–19} with differing grain sizes.²⁰ Recent experiments demonstrate the deleterious effects of GBs on carrier transport,^{10,21} and recent reports imaged graphene GBs on Cu(111)²² and Cu foil.²³ While a recent paper²⁴ reported scanning tunneling microscopy and spectroscopy (STM/S) data for GBs in graphene grown by CVD on Cu, the study was performed in ambient conditions with the graphene still on the Cu foil growth surface. Direct measurements performed under ultrahigh vacuum (UHV) conditions, and after high-temperature annealing, of the graphene GB electronic structure and carrier scattering from GBs in CVD graphene on insulators such as SiO₂ have not been reported yet.

In this work, we investigate GBs in transferred CVD graphene on SiO₂ using UHV

*Address correspondence to
jkoeple@illinois.edu,
lyding@illinois.edu.

Received for review May 10, 2012
and accepted December 13, 2012.

Published online December 13, 2012
10.1021/nn302064p

© 2012 American Chemical Society

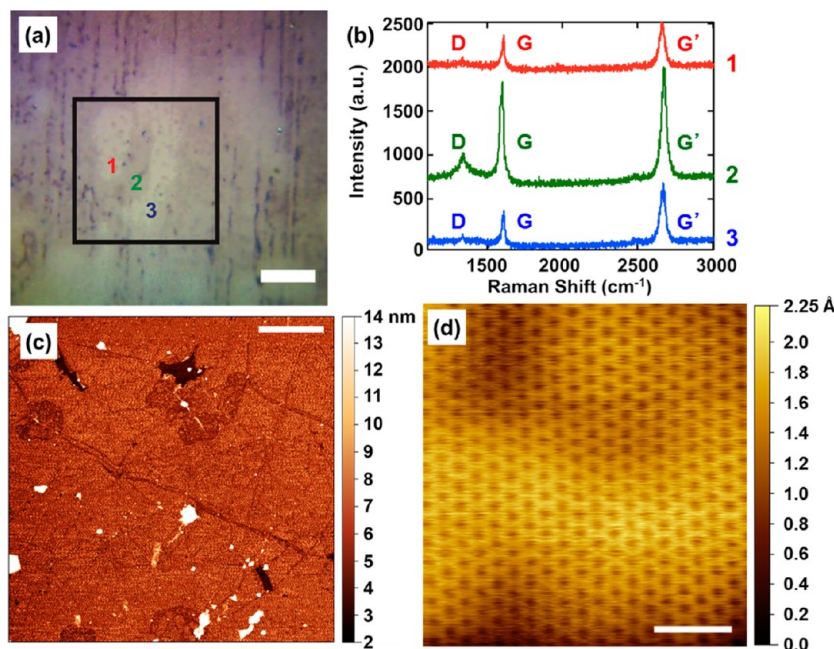


Figure 1. Graphene characterization after growth and transfer to SiO_2/Si . (a) Optical image, with location of Raman spectra indicated and a $5 \mu\text{m}$ scale bar. Contrast differences indicate regions of monolayer and bilayer graphene. (b) Raman spectra taken at the locations marked in (a) with $I(G')/I(G)$ ratios of 1.05, 1.08, and 1.88 for curves 1, 2, and 3, respectively. The curves are offset for clarity. (c) A $10 \mu\text{m} \times 10 \mu\text{m}$ tapping mode AFM scan of the graphene sample after cleaning and scanning with the STM, showing some tears in the film and some debris. The scale bar is $2 \mu\text{m}$. (d) Small STM scan of the graphene clearly showing the graphene honeycomb lattice. The scale bar is 1 nm.

scanning tunneling microscopy (UHV-STM) and spectroscopy (STS). In agreement with the recent TEM studies of graphene GBs,^{17–19} we find that the GBs are aperiodic, as expected from non-epitaxial growth on Cu. We easily distinguish GBs from the growth *versus* wrinkles caused by the growth process^{23,25} or induced post-growth by the transfer process.^{20,26} The GBs significantly alter the graphene electronic structure, with most showing enhanced empty states tunneling conductance, and lead to localized states at the GBs. Additionally, the local doping of the GBs shifts from p-type in the bulk to lower-doped p-type or n-type doping. We also observe decaying standing waves propagating in the zigzag directions and superstructures immediately adjacent to the GBs. Analyzing these patterns shows a decay length on the order of $\sim 1 \text{ nm}$. Fourier transforms of the STM images show that intervalley scattering and backscattering are the dominant scattering mechanisms from these aperiodic GBs, which lead to the decrease of carrier mobility in CVD-grown graphene.

RESULTS AND DISCUSSION

Figure 1a shows an optical image of our transferred graphene sample on SiO_2/Si . The sample displays areas of differing contrast, which we attribute to multiple graphene layers. Figure 1b gives point Raman spectra taken at the locations marked in Figure 1a, indicating definite variation in the G'/G (also called 2D/G) peak intensity ratio. The ratio for curves 1, 2, and 3 are 1.05,

1.08, and 1.88, respectively. On the basis of the optical contrast and the G'/G intensity ratios, spectrum 1 is near a monolayer and bilayer graphene transition,²⁷ spectrum 2 is bilayer graphene, and spectrum 3 is monolayer graphene. Thus, the Raman data and the optical contrast show that the growth yielded a mixture of monolayer and bilayer graphene. High-resolution STM scans of the sample reveal that the growth parameters yielded predominantly turbostratic graphene (see Supporting Information). Figure 1c shows a $10 \times 10 \mu\text{m}$ AFM scan of the graphene after transfer to the SiO_2/Si substrate and surface preparation (*i.e.*, degas at $600\text{--}700 \text{ }^\circ\text{C}$ for 24 h) for the UHV-STM system (see Methods). Clearly, there is debris remaining from the graphene growth or transfer process that was not removed during the sample preparation. The surface also displays graphene film ripples and wrinkles. The smaller line features on the surface are graphene wrinkles^{20,25,26,28} and not GBs, as they are too tall compared to GBs observed by STM. A small-area STM image shown in Figure 1d and taken in a region without wrinkles shows the characteristic graphene honeycomb lattice against the underlying SiO_2 topography.

Unlike prior STM studies of GBs in HOPG,^{29,30} the graphene GBs in CVD-grown graphene studied here are generally aperiodic. They also show no preferential misorientation angle between the different graphene domains. Further, we note that these GBs occur in regions of turbostratic bilayer graphene

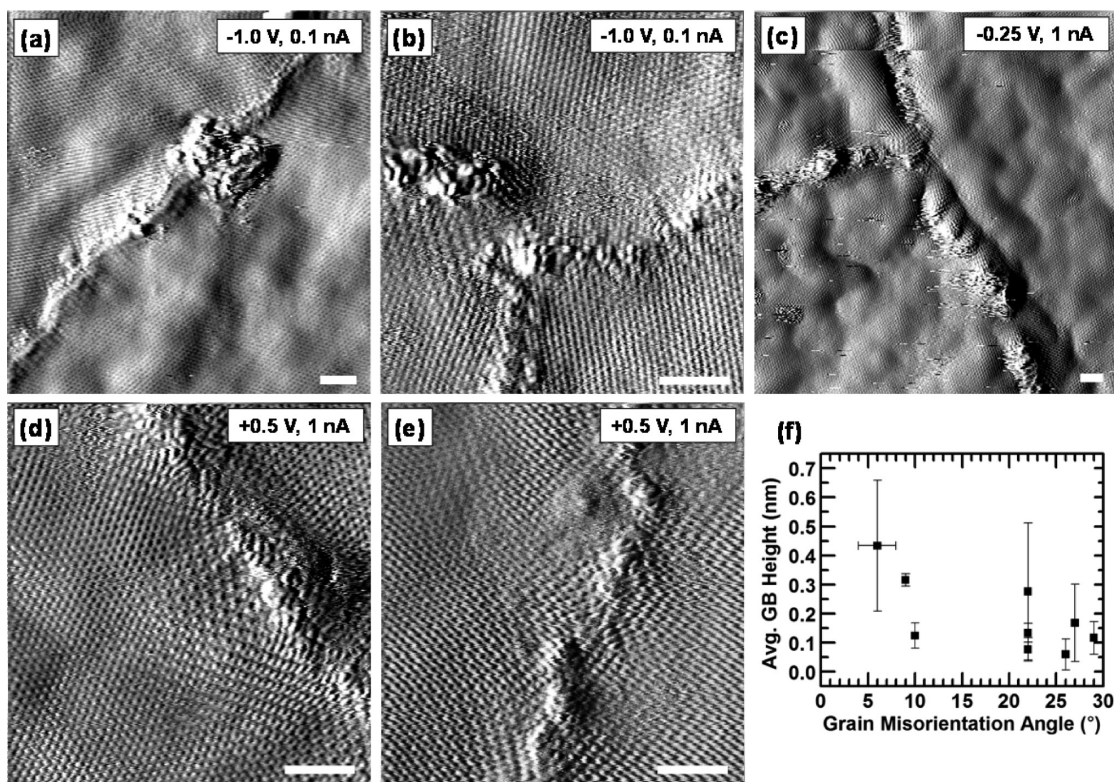


Figure 2. STM images of graphene grain boundaries (GBs). The scale bars are 2 nm. (a) STM image of a GB between two grains misoriented by $\sim 29^\circ$. The debris within the scan center is likely remnant PMMA contamination from the graphene transfer. (b) Smaller STM scan of the GBs formed at the meeting point between three different graphene grains misoriented by $\sim 9^\circ$ (lower left and top), 22° (top and lower right), and 29° (lower left and lower right), respectively. (c) Larger STM scan of a different set of GBs formed at the meeting point between three different graphene grains. The misorientation angles between the grains are $\sim 6^\circ$ (right and lower left), 20° (lower left and upper left), and 26° (upper left and right), respectively. (d) Smaller STM scan of a GB formed between two grains misoriented by $\sim 27^\circ$. Note the very clear $(\sqrt{3} \times \sqrt{3})R30^\circ$ superstructure to the left of the GB. (e) Another GB between two graphene grains misoriented by $\sim 10^\circ$. This scan also showed superstructures on both sides of the grain boundary. (f) Plot of average apparent GB height versus graphene grain misorientation angle.

(see Supporting Information). Figure 2 shows several GBs, contrast-enhanced by taking spatial derivatives of STM topographs. The misorientation angles between the graphene grains for the GBs shown in Figure 2 are $\sim 6, 9, 10, 20, 22, 26, 27$, and 29° . Due to the curvature of the graphene induced by conformation to the underlying SiO_2 surface, there is a mosaic spread of $\sim 1\text{--}2^\circ$ in the measurements. The misorientation angle between the two graphene grains shown in Figure 2a is $\sim 29^\circ$, and the resulting GB is well-ordered with the exception of transfer-induced contamination. The triple GB shown in Figure 2b illustrates the difference in disorder and structure of the GBs for three different graphene grain misorientation angles. The misorientation angle between the lower left and upper graphene grains is $\sim 9^\circ$, the upper and lower right grains is $\sim 22^\circ$, and the lower right and lower left grains is $\sim 29^\circ$, respectively. Figure 2c shows another triple GB with misorientation angles between the right and lower left, lower left and upper left, and upper left and right graphene grains of $\sim 6, 20$, and 26° , respectively. The GBs shown in Figure 2d,e have relative misorientation angles of ~ 27 and $\sim 10^\circ$, respectively. These images also have $(\sqrt{3} \times \sqrt{3})R30^\circ$ superstructures on both sides of the

GBs in each image. The comparison of the heights of the different GBs studied with grain misorientation angle displayed in Figure 2f shows that most of the GBs are around $1\text{--}2$ Å tall with the GBs with smaller misorientation angles generally having larger and more varied apparent heights in the STM. The average value for all of the GBs measured was ~ 1.9 Å. The apparent height can also vary by a few angstroms even for GBs with very similar grain misorientation angles. The error bar on the first point for the misorientation angle illustrates the variation in the graphene lattice directions due to the graphene conformation to the SiO_2 topography.

While the recent TEM studies of graphene GBs^{17–19} resolved the exact structure of some graphene GBs, the GB electronic structure information was absent. Studies of hexagonal graphene grains measuring the resistances of individual GBs^{10,21} have demonstrated their impediment to carrier transport. Here, our ultraclean, UHV-STS measurements of GBs in CVD graphene transferred to SiO_2 fill the knowledge gap between the TEM studies and the individual GB device measurements. The GBs described here (Figures 3 and 4) occur in regions of turbostratic graphene (see Supporting

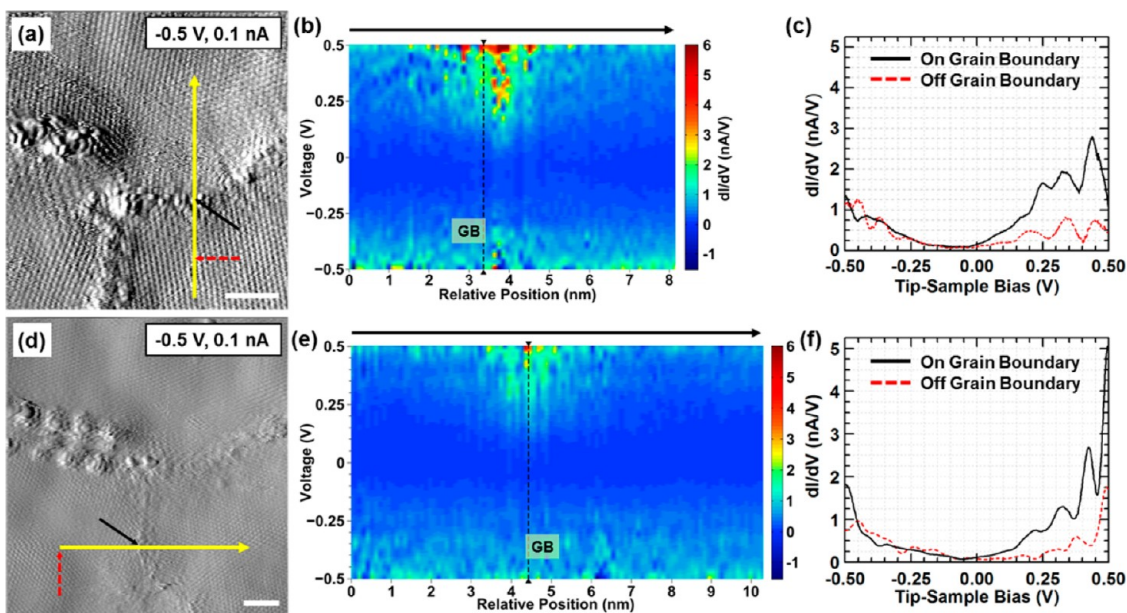


Figure 3. Scanning tunneling spectroscopy (STS) of graphene GBs. (a) STM image of the grain boundaries formed at the meeting point of three graphene grains. The yellow arrow indicates the locations of the spectra. (b) Map of tunneling conductance as a function of tip–sample bias and position from bottom to top of the arrow direction in (a). The vertical, dashed black line indicates the location of the GB. The spectra map shows a marked enhancement of the tunneling conductance in empty states at the GB. (c) Comparison of tunneling conductance for a point on the GB (solid, black line) and a point away from the GB (dashed, red line) to illustrate the enhanced empty states tunneling conductance at the GB. The solid, black and dashed, red arrows in (a) indicate the locations of the respective individual spectra shown in this plot. (d) Larger STM image of the same set of GBs as shown in (a), with the locations of the spectra across the lower GB indicated by a yellow arrow. (e) Map of tunneling conductance as a function of tip–sample bias and position from left to right along the red line shown in (d). The vertical, dashed black line in (e) also indicates the location of the GB. Again, there is a marked enhancement of the empty states tunneling conductance at the GB. (f) Comparison of tunneling conductance for a point on the GB (solid, black line) and a point away from the GB (dashed, red line) illustrating the enhancement seen in (e). The solid, black and dashed, red arrows in (d) indicate the locations of the respective individual spectra shown in this plot. The scale bars in (a) and (d) are 2 nm.

Information). Figure 3a shows the same triple GB from Figure 2b with a yellow arrow indicating the location of a I – V spectra line. The calculated tunneling conductance (dI/dV) spectra map from this spectra line is shown in Figure 3b, with a vertical, dashed black line marking the location of the GB. There is clear enhancement of empty states (dI/dV) between the spectra at and near the GB *versus* that of the graphene further away from the GB. Figure 3c compares individual (dI/dV) spectra taken on (solid, black line) and off (dashed, red line) the GB, showing strong empty states (dI/dV) enhancement at the GB. This asymmetric, enhanced empty states tunneling conductance at the GB is seen in most of the GB spectroscopy studied. Figure 3d shows a larger STM image of the same triple GB as in Figures 2b and 3a with lower resolution than in Figure 3a. The yellow arrow in Figure 3d indicates the location of a line of I – V spectra taken across the GB between the lower left and lower right graphene grains. Figure 3e shows the calculated (dI/dV) tunneling conductance map for the GB marked in Figure 3d. A vertical, dashed black line on the map indicates the GB location. Similarly, these data show enhanced empty states (dI/dV) at the GB as compared to the surrounding graphene. Individual spectra in Figure 3f highlight this observation. Constant tip–sample bias cuts of the

spectra map from Figure 3e (shown in Supporting Information Figure S4) illustrate the lateral extent of this enhancement of empty states (dI/dV). We extract decay lengths for the enhanced empty states (dI/dV) from the spectra map shown in Figure 3e, giving an average decay length on the order of 1 nm (see Supporting Information Figure S5).

To first order, normalization of the tunneling conductance by the normal conductance, or $(dI/dV)/(I/V)$, should remove the dependence on the transmission coefficient leaving the normalized surface density of states (DOS) plus a background term.³¹ Figure 4a shows the (dI/dV) spectra map from Figure 3b after normalizing the data by I/V ,³² with a vertical, dashed black line indicating the GB location. The asymmetric enhancement present in empty states for the tunneling conductance is not present after normalization by I/V . The individual point comparison in Figure 4b shows the $(dI/dV)/(I/V)$ for the same two points as the (dI/dV) comparison in Figure 3c. This point comparison reiterates that the overall, asymmetric enhancement of empty states in the (dI/dV) data at the GB is not present in the normalized data. Figure 4c,d also shows the $(dI/dV)/(I/V)$ spectra map and individual point comparison for the (un-normalized) (dI/dV) data from Figure 3e,f, respectively. Again, the vertical, dashed black line

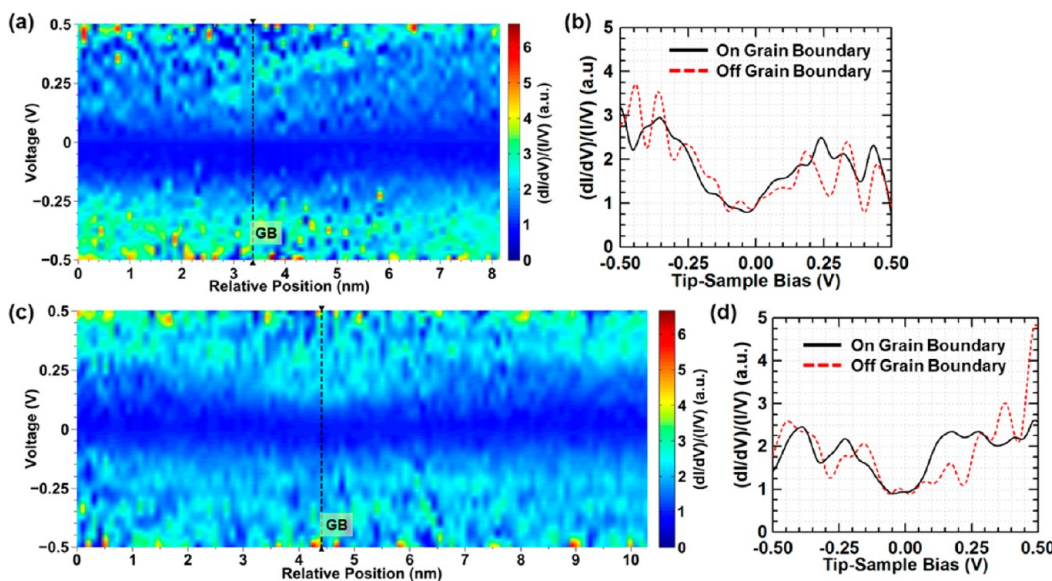


Figure 4. Normalized tunneling conductance of grain boundaries (GBs). (a) Normalized tunneling conductance map for the same spectra as the (non-normalized) tunneling conductance map from Figure 3b. The vertical, dashed black line in (a) indicates the location of the GB. The enhancement seen in empty states for the tunneling conductance data is not present when the data are normalized to the tunneling current. (b) Comparison of the normalized tunneling conductance for a point on the GB (solid, black line) and a point away from the GB (dashed, red line) illustrating the lack of any overall empty states enhancement at the GB. There is a state at (b) at approximately +0.24 V on the GB that is not present away from the GB. (c) Normalized tunneling conductance map for the same data as the (non-normalized) tunneling conductance map from Figure 3e. Here the vertical, dashed black line also indicates the location of the GB. Again, the strong enhancement seen in empty states for the (non-normalized) tunneling conductance data from Figure 3e is not present when the data are normalized to the tunneling current. (d) Normalized tunneling conductance comparison for a point on the GB (solid, black line) and a point away from the GB (dashed, red line). There is no overall enhancement in empty states at the GB as there was for the non-normalized tunneling conductance. However, there is a state at approximately +0.15 V at the GB, which is not present away from it.

indicates the GB location. The normalization of this data also removes the asymmetric, empty states enhancement present at the GB in the (un-normalized) (dI/dV) . The $I-V$ spectra for both GBs in Figures 3 and 4 also show higher current in empty states on the GBs than on the surrounding graphene. This removal of the enhanced empty states (dI/dV) present at the GBs upon normalization by I/V suggests that the asymmetric, enhanced empty states (dI/dV) at the GBs arises from a tunneling transmission coefficient effect due to a change in apparent barrier height at the GBs. The spectra map in Figure 4c also shows localized states near the GB at approximately +0.15 V that decay away from the GB. The individual $(dI/dV)/(I/V)$ point comparison in Figure 4d also shows these states at the GB near +0.15 V that are not present away from the GB. This implies that the states are a local property of this particular GB. The presence of localized states at and near the GB in the data from Figures 4c–d is consistent with observations on periodic GBs in HOPG, whose localized states depend on the GB structure.^{29,30} We note that the “oscillations” visible in the individual (dI/dV) and $(dI/dV)/(I/V)$ spectra in Figures 3c, 3f, 4b, and 4d are from noise in the original $I-V$ spectra from which the (dI/dV) are calculated and are not from Landau levels caused by strain within the graphene.³³ We also note that our energy resolution is limited by

the room-temperature measurements to ~ 50 meV, typical for thermal broadening at room temperature in the STM sample and tip.

Since no pronounced secondary minima are present in the (dI/dV) spectra shown in Figure 3, the minimum of the (dI/dV) corresponds to the Dirac point.³⁴ The plot in Figure 5a shows the tip–sample bias of the minimum of the (dI/dV) spectra from the line of spectra across the GB from Figure 3d, which has a misorientation angle of $\sim 29^\circ$ and an average apparent height of 0.12 nm. From the Gaussian fit (red line), the Dirac point on the GB occurs at -0.044 V and the value in the surrounding graphene away from the GB is $+0.057$ V. We convert these Dirac point values to charge-carrier concentration using the equation $n = (E_D^2)/(\pi\hbar^2 v_F^2)$, where E_D is the energy of the Dirac point, \hbar is Planck's constant divided by 2π , and n is the carrier concentration, and v_F is the Fermi velocity ($v_F = 10^6$ m/s). We note that this is a fair first order estimate of the doping.^{15,24,35} This gives a p-type doping of 2.4×10^{11} cm $^{-2}$ in the bulk graphene away from the GB and an n-type doping of 1.4×10^{11} cm $^{-2}$ at the GB. The full width at half-maximum for this doping change from the Gaussian fit is ~ 3.6 nm. So the GB from Figure 3d shifts the doping from p-type to n-type, creating a *p-n-p* junction and changing the local work-function over a distance of ~ 3.6 nm.

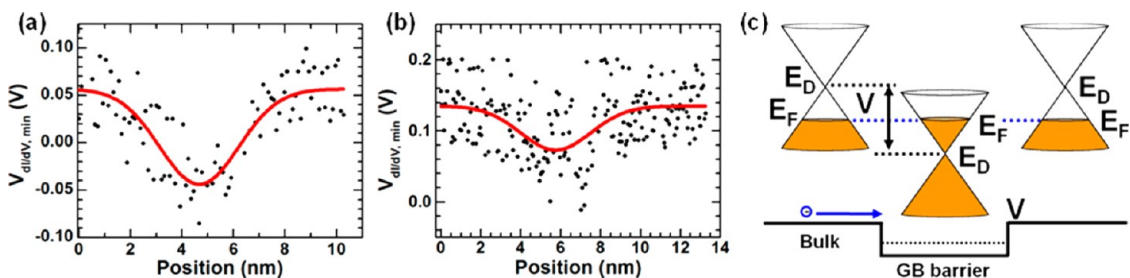


Figure 5. Voltage of (dI/dV) minimum versus position showing a barrier at the grain boundary. (a) Plot of tip–sample bias (V) of the (dI/dV) minimum at each point in the line of STS across the GB from Figure 3d. The shift of the minimum here indicates a transition from p-type doping in the bulk to n-type doping at the GB. (b) Plot of tip–sample bias (V) of the minimum of the (dI/dV) at each point in a line of STS across the GB from Figure 2d also showing a shift toward n-type doping. (c) Diagram illustrating the shift in doping caused by the presence of the GB. This one illustrates a p - n - p doping shift.

Similarly, Figure 5b shows the tip–sample bias of the minimum of the spectra from a line of spectra across the GB from Figure 2d. The GB from Figure 2d has a misorientation angle of $\sim 27^\circ$ and an average apparent height of 0.17 nm. The Gaussian fit (red line) for this data gives a Dirac point in the bulk graphene away from the GB of +0.13 V and a Dirac point on the GB of +0.073 V. The full width at half-maximum of this Gaussian fit is ~ 4.2 nm. These correspond to p-type doping of $1.3 \times 10^{12} \text{ cm}^{-2}$ in the bulk graphene away from the GB and p-type doping of $3.9 \times 10^{11} \text{ cm}^{-2}$ at the GB. Hence this second GB has p - p' - p doping ($p' < p$). In both cases, the presence of the GB shifts the doping toward n-type from the bulk, or decreases the work function. This decrease in work function would modify the apparent tunneling barrier height and affect the tunneling transmission coefficient.

Our results show that the modified topological structure of the GBs leads localized states and decreases the work function. Normalization of the (dI/dV) spectra by I/V suggests that the observation of enhanced empty states (dI/dV) at the GBs arises from transmission coefficient change due to a change in apparent tunneling barrier height, as would occur with the measured work function change at the GBs. Supporting Information Figure S6 contains a plot illustrating how a shift in doping, with a decrease in work function, could lead to the observed enhanced empty states (dI/dV) at the GBs described in Figures 3 and 4. Furthermore, a recent STS study of N-doped CVD graphene also observed enhanced empty states (dI/dV) near the sites of the dopants compared to the undoped CVD graphene.³⁶ The Supporting Information contains spectroscopy of GBs in CVD graphene on mica with water trapped between the graphene and the mica.³⁷ The GBs on this surface, which does not have the same charge puddling as graphene on SiO_2/Si ,^{38,39} also have doping shifts and potential barriers. Supporting Information Figure S7 shows a large-angle GB with a barrier of ~ 0.06 V that shifts the doping from p-type to n-type (see Supporting Information). Depending on the GB topology, the misorientation angle, and the background doping of the bulk graphene, the

shift in the work function can lead to the formation of a graphene p - n - p junction (Figure 5c), where the transition between the doping levels occurs over a width of ~ 1.8 – 2.1 nm. We note that the length scale for this doping shift associated with the GBs is ~ 1 – 2 nm, while the length scale associated with the doping fluctuations due to charge puddling of graphene on SiO_2/Si is closer to 10–20 nm or more.^{38,39}

Spectroscopy of a small-angle GB in a region of monolayer CVD graphene on mica with water trapped between the graphene and the mica (Supporting Information Figure S8) suggests that local states may also play a role in the enhanced empty states (dI/dV) at the GB. The particular GB in Supporting Information Figure S8 has a very small potential barrier on the order of the thermal voltage, ~ 0.026 V, but has slightly higher (dI/dV) on the GB for both filled and empty states than the surrounding graphene grains. Since there is only a thermally negligible doping shift at the GB, local states at the GB must lead to the symmetric, locally enhanced (dI/dV). See the Supporting Information and Figures S10 and S11 for spectroscopic data on back-gated graphene GBs on SiO_2/Si .

In addition to topographic and spectroscopic information, the STM can also study carrier scattering in graphene^{40,41} by observing electronic superstructures induced by defects, adsorbates, or edges. We achieve this by means of fast Fourier transforms (FFTs) and FFT filtering, which elucidate carrier scattering from the graphene GBs.^{40,41} Figure 6a shows a topographic STM image of a GB between two graphene grains misoriented by $\sim 29^\circ$, with the grain to the left of the GB labeled "L" and the grain to the right of the GB labeled "R." The false-colored STM topographic derivative given in Figure 6b provides better contrast of the graphene lattice. From this, a linear superstructure is apparent on both the left and right sides of the GB, and these superstructures propagate in different directions on each side of the GB. The top panel of Figure 6c shows a small section (dashed, cyan box) of the image shown in Figure 6b, taken to the left of the GB, and its resulting 2D FFT, showing the six bright outer points characteristic of the graphene reciprocal lattice.

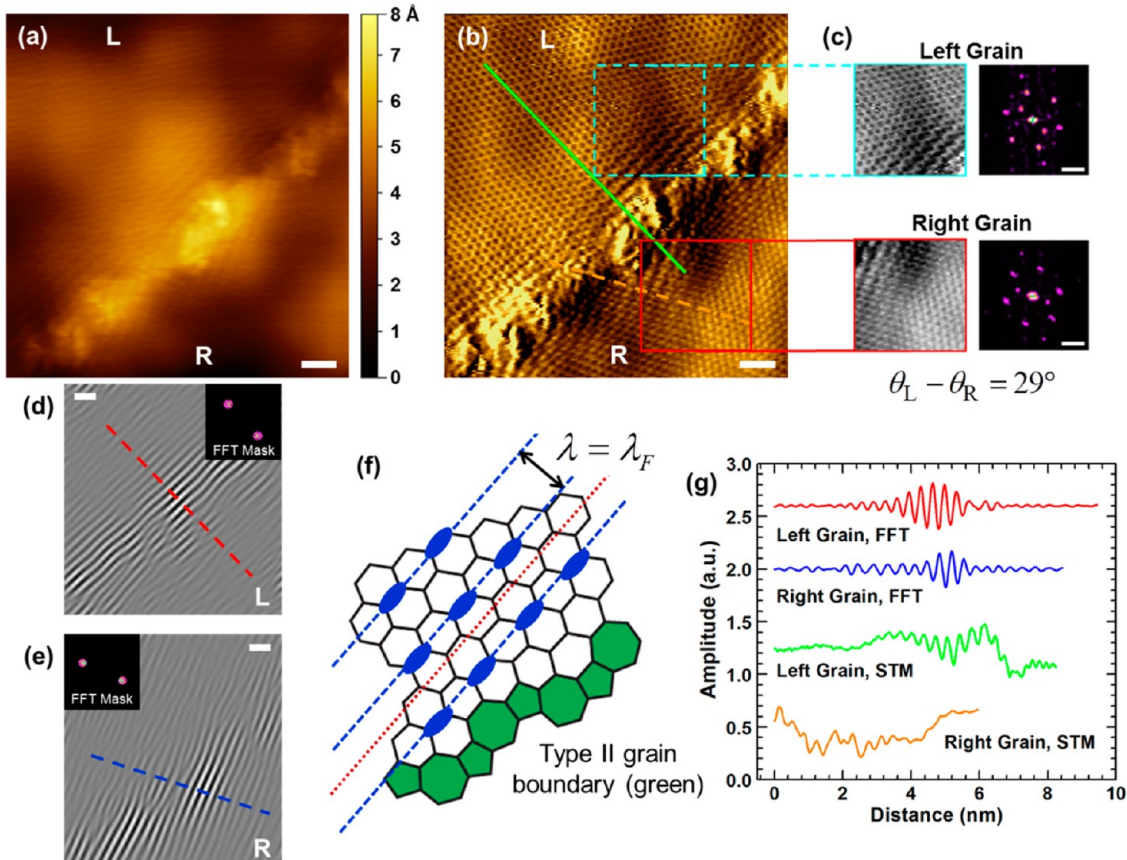


Figure 6. Linear superstructure analysis. (a) STM image of a GB between two graphene grains with a misorientation angle of $\sim 29^\circ$, showing a linear superstructure observed on either side of the GB. (b) False-colored derivative of the STM topograph shown in (a) for better contrast. (c) Upper panel shows a section to the left (L) of the GB and the resulting 2D FFT. The six outer points forming a hexagon correspond to the reciprocal lattice of the graphene; the pair of inner points corresponds to the linear superstructure observed immediately adjacent to left of the GB. Lower panel shows a section to the right (R) of the GB and the resulting 2D FFT, similar to the upper panel. (d) FFT filtered version of the L image from (b) using the inset FFT mask, which filters out everything but the linear superstructure. (e) FFT filtered version of the R image from (b) using the inset FFT mask, which corresponds to filtering out everything but the linear superstructure. (f) Schematic model of the left side of a pentagon-heptagon GB, similar to the one shown in (a,b), but with a different misorientation angle. The blue regions illustrate the interference localization along the C-C bonds, giving a superstructure wavelength λ_F (Fermi wavelength). (g) Superstructure spatial extent, with line cuts taken perpendicular to the wavefront and offset for clarity. The two curves labeled with left and right grain FFT were extracted along the lines shown in (d) and (e), respectively. The two curves labeled with STM were extracted along the lines shown in (b). The decay length of the linear superstructure is ~ 1.01 nm in the left grain and ~ 0.49 nm in the right grain. The scale bars are all 1 nm.

Similarly, the bottom panel of Figure 6c shows a small section to the right of the GB from Figure 6b and the resulting 2D FFT. These two FFTs also have a pair of inner points that correspond to K and K' points of the graphene Brillouin zone (BZ) on their respective GB sides.⁴⁰

By following the 2D FFT filtering procedure in the Supporting Information and in Yang *et al.*,⁴¹ we filtered everything but the linear superstructure patterns on the left and right sides of the GB, leaving only the linear superstructures. Figure 6d,e shows the filtering results for the linear superstructure in the left and right graphene grains, respectively, with the FFT masks that we use shown in the inset. While the propagation direction of the linear superstructure to the left of the GB in Figure 6b is close to perpendicular to the GB ($\sim 83^\circ$), the angle between the propagation direction

of the linear superstructure to the right of the GB in Figure 6c and the GB is $\sim 54^\circ$. The superstructure propagation direction in each grain is along one of the zigzag directions in that graphene grain. From the image in Figure 6b and the FFTs and filtered images in Figure 6c,d, we find that the period of this linear superstructure is ~ 3.7 Å. This is approximately the Fermi wavelength, $\lambda_F = 3a/2 = 3.69$ Å, where $a = 2.46$ Å is the lattice constant of graphene. Such a value was reported for linear superstructures observed adjacent to irregular armchair graphene edges on SiC.⁴¹

The observation of λ_F rather than $\lambda_F/2$ indicates that the interference of the scattered carriers is localized along the C-C bonds, where there are available DOS.⁴¹ In contrast, the recent work of Tian *et al.*⁴² observed a linear superstructure with period $\lambda_F/2$ adjacent to an armchair graphene edge on Cu, suggesting that the

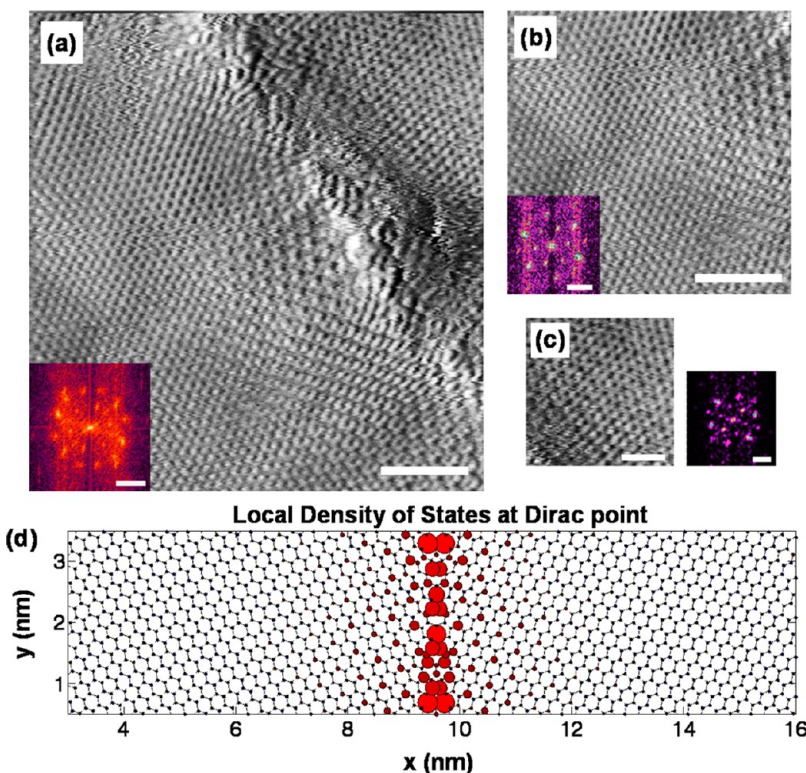


Figure 7. Intervalley scattering from a grain boundary (GB). (a) STM image of a GB between two graphene grains with a misorientation angle of $\sim 27^\circ$, showing a $(\sqrt{3} \times \sqrt{3})R30^\circ$ superstructure to the left of the GB. The lower left inset shows the FFT of the entire image. (b) Cropped lower left section of the STM scan (same scale) shown in (a) with just the graphene lattice and the superstructure. The inset FFT in the lower left corner shows all six points of the Brillouin zone (BZ). (c) Cropped upper right section of the STM scan from (a) shown at the same scale. The FFT of the image also shows all six points of the BZ. (d) Tight-binding simulation of a GB with 21.8° grain misorientation showing the local density of states at the Dirac point and exhibiting a $(\sqrt{3} \times \sqrt{3})R30^\circ$ superstructure pattern. The scale bars in (a) and (b) are 2 nm. The scale bar in (c) is 1 nm. The FFT scales bar in (a), (b), and (c) are 4 nm^{-1} .

substrate electronic structure allows the interference of the scattered carriers to localize in positions off the graphene C–C bonds. The schematic shown in Figure 6f illustrates the localization of carrier interference on one side of a type II GB¹⁴ for a GB where the two grains are misoriented by $\sim 32^\circ$. Since the graphene grains are rotationally misoriented, the direction of the localization would be different on the other side of the GB, matching our observation for the GB in Figure 6a.

The observation of a linear superstructure adjacent to the GB shown in Figure 6a additionally suggests that each of the graphene grains has an irregular armchair edge at the point where the defects forming the GB start.⁴¹ Furthermore, the pair of interior points in the FFT taken on either side of the GB indicates that the primary scattering mode for such GBs is back-scattering.⁴⁰ Figure 6g shows line cuts taken on the left and right sides of the GB for the filtered images shown in Figure 5b,c and the topographic derivative shown in Figure 6b. Fitting the peaks of the interference patterns for the line cuts from the filtered images in Figure 6d,e (the red and blue curves) to a decaying exponential function gives decay lengths of $\sim 1.02 \pm 0.10 \text{ nm}$ on the left side of the GB and $\sim 0.49 \pm 0.29 \text{ nm}$

on the right side of the GB. These decay lengths are on the order of 1 nm and match the order of the average decay lengths of the enhanced empty states tunneling conductance shown in Supporting Information Figure S5 for the GB from Figure 3d–f. They are also on the same order of magnitude as the doping shifts observed at the GBs. This suggests that these decay lengths depend on the electronic structure of the GBs rather than solely thermal effects or energy spread.^{41,43}

Other GBs predominantly exhibit a $(\sqrt{3} \times \sqrt{3})R30^\circ$ superstructure on either side of the GB, as illustrated in Figure 2d,e and Figure 7 (though the pattern is more dominant along one of the zigzag directions than the other two in Figure 2d and Figure 7). In these cases, the FFTs of the STM images show a set of points corresponding to all six K and K' points of the graphene BZ. The presence of all six points of the graphene BZ indicates that intervalley scattering is allowed between all K and K' points.⁴⁰ Figure 7a shows an STM image of the same GB shown in Figure 2d, which has two graphene grains misoriented by $\sim 27^\circ$, with a 2 nm scale bar. There is a clear $(\sqrt{3} \times \sqrt{3})R30^\circ$ structure present on the left side of the GB. The inset image is the 2D FFT of the STM image. The FFT shows the expected two sets of six outer points corresponding to the

graphene reciprocal lattices on the left and right sides of the GB. There is also a set of six interior points forming a hexagon that correspond to the six K and K' points of the BZ for the graphene grain to the left of the GB, arising from the $(\sqrt{3} \times \sqrt{3})R30^\circ$ superstructure resolved to the left of the GB. The superstructure from the right side of the GB is faint in the FFT since there is only a small section of the right side of the GB present in the STM image compared to the left side of the GB.

The STM image shown in Figure 7b is a smaller section of the STM image shown in Figure 7a taken from the left side of the GB with the same scale. The scale bar is 2 nm. The inset 2D FFT shows the outer set of six points for the left grain graphene reciprocal lattice and all six points corresponding to the BZ. Similarly, Figure 7c shows a smaller section of the STM image from Figure 7a taken on the right side of the GB with the same scale and its corresponding 2D FFT. The scale bar for this image is 1 nm. The FFT of the graphene to the right of the GB in Figure 7c also shows a set of six out points corresponding to the reciprocal lattice of the right grain and all six interior points corresponding to the BZ. Since the FFTs on both sides of the GB show all six points of their respective BZs, this GB causes intervalley carrier scattering.^{40,41} The results shown in Figure 6 and Figure 7 indicate that the local structure of the GBs affect the particular nature of the carrier scattering from the GBs.

Recent work studying mesoscopic GB transport inferred intervalley carrier scattering at the GBs from a highly localized D peak in Raman spectroscopy at the GB and from the observed intergrain weak localization.^{10,21} Two recent STM studies of CVD graphene while still on the Cu growth surface^{23,24} also found the $(\sqrt{3} \times \sqrt{3})R30^\circ$ superstructures adjacent to GBs that indicate intervalley scattering from the GBs. A further STM study of graphene islands grown on Cu foil showed prominent linear superstructure from abrupt step edges (graphene–Cu) with a smaller period ($\lambda_F/2$ rather than λ_F).⁴² Thus transferring the graphene to an insulating substrate is important because the conducting Cu substrate can alter the allowed carrier interference localization. This could obscure the scattering mechanisms in a technologically relevant graphene device with GBs. Our observation of intervalley scattering of carriers from the GBs is consistent with these prior studies. However, depending on the GB structure, we also find carrier backscattering from the GBs. These results indicate that the local GB topography (e.g., heptagons, pentagons, and strained hexagons or any possible chemisorbed species) and grain misorientation dictate the predominant carrier scattering modes from that GB.

While our GBs showed evidence of intervalley scattering and backscattering, as seen in Figure 6 and Figure 7, we note that most of these observed GBs occurred on turbostratic bilayer graphene (see

Supporting Information). Supporting Information Figure S2 shows the Moiré patterns observed in the graphene grains, highlighting the turbostratic stacking. From the extracted Moiré patterns' periods, we find that the rotational misorientation of the top and bottom layers is $\sim 8.5\text{--}9.5^\circ$. Theoretical and experimental studies of turbostratic graphene⁴⁴ and graphene grown on the carbon face of SiC^{45,46} show that multilayer graphene behaves like stacked monolayer graphene when the layers are misoriented by more than 5° . Indeed, a study of turbostratically stacked few-layer graphene grown by CVD on polycrystalline Ni also showed that for layers misoriented by greater than $\sim 3^\circ$ carriers still exhibited Landau level spectra indicative of massless Dirac fermions.⁴⁷ Furthermore, the plot of the local density of states (LDOS) at the Dirac point from our tight-binding simulation of a type II GB in monolayer graphene shown in Figure 7d shows a $(\sqrt{3} \times \sqrt{3})R30^\circ$ superstructure (see Supporting Information). This confirms our observation of $(\sqrt{3} \times \sqrt{3})R30^\circ$ superstructures adjacent to most of the graphene GBs. Thus, the observed backscattering and intervalley scattering arise from the sharp lattice defects forming the GBs and not from any turbostratic interlayer interaction.

Although we do not know the exact topological structure of the GBs in Figures 6 and 7, we can make some comparative observations about the two in an attempt to determine how the local structure affects the nature of the carrier scattering. Both GBs are formed by the merging of two graphene grains with a large misorientation angle ($\sim 29^\circ$ for Figure 6 and $\sim 27^\circ$ for Figure 7). The electronic superstructures adjacent to each of the GBs extend approximately the same distance on either side of each GB and have approximately the same intensity. However, the scattering for the GB in Figure 6 is dominated by backscattering, and that for the GB in Figure 7 is intervalley scattering. The GB in Figure 6 seems to be a continuous line of defects, while the GB in Figure 7 has more of a semiperiodic structure with flat regions between regions that protrude more from the surface.

The small-angle GB ($\sim 6^\circ$) in CVD graphene on mica with water trapped between the graphene and the mica³⁷ shown in Supporting Information Figure S8 is more periodic than the GBs given in Figures 6 and 7. The electronic superstructures adjacent to the GB in Figure S8 are also much fainter. This matches with the lack of a substantial potential barrier at this GB (see Supporting Information Figure S8c). Of the GBs shown in Figures 6, 7, S7, and S8, the GB from Figure 6 had the largest potential barrier of ~ 0.1 V. The GB in Figure S8 had the smallest potential barrier of ~ 0.02 V. These data suggest that the GBs which are more periodic and well-ordered like that in Supporting Information Figure S8 will have reduced carrier scattering from the GB compared to the aperiodic GBs.

composed of a continuous line of defects (such as that in Figure 6).

CONCLUSIONS

In summary, we have studied GBs at the atomic scale using UHV-STM and STS for graphene grown by CVD on polycrystalline Cu foil and transferred to SiO_2 . We have found that no preferred misorientation angle occurs between the as-grown graphene grains. The GBs are aperiodic, in agreement with recent TEM studies of Cu-grown graphene GBs,^{17–19} and have varying heights, with an average value of 1.9 Å. As expected, the GBs strongly perturb the electronic structure of the graphene, and the GBs show an asymmetric, enhanced empty states tunneling conductance with a decay length of ~ 1 nm on either side of the GB. Graphene GBs decrease the local work

function, leading to p - n - p and p - p' - p ($p' < p$) potential barriers that act as scatterers. Fourier analysis indicates that the GB potential barriers give both backscattering and intervalley carrier scattering, deleterious for applications involving carrier transport through polycrystalline graphene films. Combining the spectroscopic and scattering results suggest that GBs that are more periodic and well-ordered lead to reduced scattering from the GBs. Recent reported work⁴⁸ suggests that GBs may actually improve the performance of polycrystalline graphene chemical sensors. This suggests GB-selective chemistry to preferentially adsorb molecules at the GBs and mitigate the potential barrier from the GBs. Alternatively, GBs could engineer doping on the nanometer scale, enabling further studies of novel physics such as Klein tunneling^{49–51} and novel devices such as a Veselago lens.⁵²

METHODS

STM Measurements. A summary of our experimental methods were published in a recent report.⁵³ In brief, our experiments used a home-built, room-temperature ultrahigh vacuum scanning tunneling microscope (UHV-STM) with a base pressure of 3×10^{-11} Torr⁵⁴ and electrochemically etched tungsten tips. Using direct-current heating through the n^+ Si substrate, we degassed the sample in the UHV-STM system at a temperature of 600–700 °C for 24 h. In our system, the tip is grounded and the bias is applied to the sample. The current set points for the constant current topographs range from 0.1–1 nA with tip–sample biases between ± 0.2 and ± 1 V. We probed the local density of states (LDOS) of the sample using constant-spacing scanning tunneling spectroscopy (STS) in which the tip feedback is turned off at predetermined locations and the tip–sample bias swept through a specified range while recording the tunneling current. We measured the graphene grain misorientation angles from the rotation of the 2D FFT patterns of each graphene grain and from fitting lines to the zigzag directions of each graphene grain using the derivative of the STM topographs.

Graphene Growth and Characterization. We grew the graphene on 1.4 mil copper foil purchased from Basic Copper in an Atomate CVD system. The foils were annealed at 1000 °C under Ar/H_2 flow for 45 min, and graphene was subsequently grown under a 17:1:3 ratio of $\text{CH}_4/\text{H}_2/\text{Ar}$ flow for 30 min at an operating pressure of 2 Torr. The resulting substrates were cooled to room temperature at ~ 20 °C/min under the same gas flow. After growth, the graphene was transferred onto a 90 nm SiO_2/n^+ Si substrate by first coating the graphene with a bilayer of 495K A2 and 950K A4 PMMA (MicroChem). Each PMMA layer was applied at 3000 rpm for 30 s followed by a 2 min bake at 200 °C. An O_2 RIE plasma removed the uncoated graphene on the backside of the Cu foil before etching the Cu foil in 1 M FeCl_3 overnight. The remaining graphene film was rinsed in deionized (DI) water to remove residual etchant before transferring to the SiO_2/Si substrate.⁴⁸ A single gold contact was shadow evaporated onto the sample to allow the STM electrical access to the graphene. After STM data were collected, we used Raman spectroscopy and atomic force microscopy (AFM) to characterize the graphene topography and quality. Raman spectroscopy was performed at 633 nm laser excitation using a Renishaw inVia Raman microscope. AFM data were collected using a Digital Instruments Veeco AFM with a Dimension IV controller.

Conflict of Interest: The authors declare no competing financial interest.

Acknowledgment. This work was supported by the Office of Naval Research through Grants N00014-06-10120 and N00014-09-0180, the Advanced Research Project Agency and

Space and Naval Warfare Center under Contract N66001-08-C-2040, the National Science Foundation under Grant CHE 10-38015, the Nanoelectronics Research Initiative, the Beckman Foundation (J.W.), and the NDSEG Graduate Fellowship (D.E. and J.W.). We acknowledge helpful conversations with Prof. Nadya Mason, Dr. Bruno Uchoa, and Prof. David Ferry. We also thank Dr. Scott Schmucker for useful conversations and assistance with the STM software.

Supporting Information Available: Further discussion of the multilayer graphene, Moiré patterns, ripping the top graphene layer and their accompanying STM images are available. Analysis of the (dI/dV) spectra map in Figure 3e to obtain the decay length of the empty states enhancement at the GB and an illustration of the effect of a graphene doping shift on tunneling conductance are also available. Further STS data for GBs on mica and back-gated GBs on SiO_2/Si , and a description of the tight-binding simulation of a periodic GB are available. This material is available free of charge via the Internet at <http://pubs.acs.org>.

Note Added in Proof: During the review process, we became aware of a related computational study that further corroborates the deleterious effects of GBs on carrier transport (ref 55).

REFERENCES AND NOTES

- Castro Neto, A. H.; Guinea, F.; Peres, N. M. R.; Novoselov, K. S.; Geim, A. K. The Electronic Properties of Graphene. *Rev. Mod. Phys.* **2009**, *81*, 109–162.
- Berger, C.; Song, Z.; Li, T.; Li, X.; Ogbazghi, A. Y.; Feng, R.; Dai, Z.; Marchenkov, A. N.; Conrad, E. H.; First, P. N.; et al. Ultrathin Epitaxial Graphite: 2D Electron Gas Properties and a Route toward Graphene-Based Nanoelectronics. *J. Phys. Chem. B* **2004**, *108*, 19912–19916.
- Unarunotai, S.; Koepke, J. C.; Tsai, C.; Du, F.; Chialvo, C. E.; Murata, Y.; Haasch, R.; Petrov, I.; Mason, N.; Shim, M.; et al. Layer-by-Layer Transfer of Multiple, Large Area Sheets of Graphene Grown in Multilayer Stacks on a Single SiC Wafer. *ACS Nano* **2010**, *4*, 5591–5598.
- Reina, A.; Jia, X.; Ho, J.; Nezich, D.; Son, H.; Bulovic, V.; Dresselhaus, M. S.; Kong, J. Large Area, Few-Layer Graphene Films on Arbitrary Substrates by Chemical Vapor Deposition. *Nano Lett.* **2009**, *9*, 30–35.
- Sutter, P. W.; Flege, J.; Sutter, E. A. Epitaxial Graphene on Ruthenium. *Nat. Mater.* **2008**, *7*, 406–411.
- Li, X.; Cai, W.; An, J.; Kim, S.; Nah, J.; Yang, D.; Piner, R.; Velamakanni, A.; Jung, I.; Tutuc, E.; et al. Large-Area Synthesis of High-Quality and Uniform Graphene Films on Copper Foils. *Science* **2009**, *324*, 1312–1314.

7. Coraux, J.; N'Diaye, A. T.; Busse, C.; Michely, T. Structural Coherency of Graphene on Ir(111). *Nano Lett.* **2008**, *8*, 565–570.
8. Land, T. A.; Michely, T.; Behm, R. J.; Hemminger, J. C.; Comsa, G. STM Investigation of Single Layer Graphite Structures Produced on Pt(111) by Hydrocarbon Decomposition. *Surf. Sci.* **1992**, *264*, 261–270.
9. Wofford, J. M.; Nie, S.; McCarty, K. F.; Bartelt, N. C.; Dubon, O. D. Graphene Islands on Cu Foils: The Interplay between Shape, Orientation, and Defects. *Nano Lett.* **2010**, *10*, 4890–4896.
10. Yu, Q.; Jauregui, L. A.; Wu, W.; Colby, R.; Tian, J.; Su, Z.; Cao, H.; Liu, Z.; Pandey, D.; Wei, D.; et al. Control and Characterization of Individual Grains and Grain Boundaries in Graphene Grown by Chemical Vapour Deposition. *Nat. Mater.* **2011**, *10*, 443–449.
11. Li, X.; Magnuson, C. W.; Venugopal, A.; Tromp, R. M.; Hannon, J. B.; Vogel, E. M.; Colombo, L.; Ruoff, R. S. Large-Area Graphene Single Crystals Grown by Low-Pressure Chemical Vapor Deposition of Methane on Copper. *J. Am. Chem. Soc.* **2011**, *133*, 2816–2819.
12. Vlassiouk, I.; Regmi, M.; Fulvio, P.; Dai, S.; Datskos, P.; Eres, G.; Smirnov, S. Role of Hydrogen in Chemical Vapor Deposition Growth of Large Single-Crystal Graphene. *ACS Nano* **2011**, *5*, 6069–6076.
13. Wood, J. D.; Schmucker, S. W.; Lyons, A. S.; Pop, E.; Lyding, J. W. Effects of Polycrystalline Cu Substrate on Graphene Growth by Chemical Vapor Deposition. *Nano Lett.* **2011**, *11*, 4547–4554.
14. Yazyev, O. V.; Louie, S. G. Electronic Transport in Polycrystalline Graphene. *Nat. Mater.* **2010**, *9*, 806–809.
15. Yazyev, O. V.; Louie, S. G. Topological Defects in Graphene: Dislocations and Grain Boundaries. *Phys. Rev. B* **2010**, *81*, 195420.
16. Liu, Y.; Yakobson, B. I. Cones, Pringles, and Grain Boundary Landscapes in Graphene Topology. *Nano Lett.* **2010**, *10*, 2178–2183.
17. Huang, P. Y.; Ruiz-Vargas, C.; van der Zande, A. M.; Whitney, W. S.; Levendorf, M. P.; Kevek, J. W.; Garg, S.; Alden, J. S.; Hustedt, C. J.; Zhu, Y.; et al. Grains and Grain Boundaries in Single-Layer Graphene Atomic Patchwork Quilts. *Nature* **2011**, *469*, 389–392.
18. An, J.; Voelkl, E.; Suk, J. W.; Li, X.; Magnuson, C. W.; Fu, L.; Tiemeijer, P.; Bischoff, M.; Freitag, B.; Popova, E.; et al. Domain (Grain) Boundaries and Evidence of “Twinlike” Structures in Chemically Vapor Deposited Grown Graphene. *ACS Nano* **2011**, *5*, 2433–2439.
19. Kim, K.; Lee, Z.; Regan, W.; Kisielowski, C.; Crommie, M. F.; Zettl, A. Grain Boundary Mapping in Polycrystalline Graphene. *ACS Nano* **2011**, *5*, 2142–2146.
20. Nemes-Incze, P.; Yoo, K. J.; Tapasztó, L.; Dobrik, G.; Lábár, J.; Horváth, Z. E.; Hwang, C.; Biró, L. P. Revealing the Grain Structure of Graphene Grown by Chemical Vapor Deposition. *Appl. Phys. Lett.* **2011**, *99*, 023104.
21. Jauregui, L. A.; Cao, H.; Wu, W.; Yu, Q.; Chen, Y. P. Electronic Properties of Grains and Grain Boundaries in Graphene Grown by Chemical Vapor Deposition. *Solid State Commun.* **2011**, *151*, 1100–1104.
22. Gao, L.; Guest, J. R.; Guisinger, N. P. Epitaxial Graphene on Cu(111). *Nano Lett.* **2010**, *10*, 3512–3516.
23. Zhang, Y.; Gao, T.; Gao, Y.; Xie, S.; Ji, Q.; Yan, K.; Peng, H.; Liu, Z. Defect-like Structures of Graphene on Copper Foils for Strain Relief Investigated by High-Resolution Scanning Tunneling Microscopy. *ACS Nano* **2011**, *5*, 4014–4022.
24. Tapasztó, L.; Nemes-Incze, P.; Dobrik, G.; Yoo, K. J.; Hwang, C.; Biró, L. P. Mapping the Electronic Properties of Individual Graphene Grain Boundaries. *Appl. Phys. Lett.* **2012**, *100*, 053114.
25. Pan, Z.; Liu, N.; Fu, L.; Liu, Z. Wrinkle Engineering: A New Approach to Massive Graphene Nanoribbon Arrays. *J. Am. Chem. Soc.* **2011**, *133*, 17578–17581.
26. Liu, N.; Pan, Z.; Fu, L.; Zhang, C.; Dai, B.; Liu, Z. The Origin of Wrinkles on Transferred Graphene. *Nano Res.* **2011**, *4*, 996–1004.
27. Ferrari, A. C.; Meyer, J. C.; Scardaci, V.; Casiraghi, C.; Lazzeri, M.; Mauri, F.; Piscanec, S.; Jiang, D.; Novoselov, K. S.; Roth, S.; et al. Raman Spectrum of Graphene and Graphene Layers. *Phys. Rev. Lett.* **2006**, *97*, 187401.
28. Ruiz-Vargas, C.; Zhuang, H. L.; Huang, P. Y.; van der Zande, A. M.; Garg, S.; McEuen, P. L.; Muller, D. A.; Hennig, R. G.; Park, J. Softened Elastic Response and Unzipping in Chemical Vapor Deposition Graphene Membranes. *Nano Lett.* **2011**, *11*, 2259–2263.
29. Červenka, J.; Flipse, C. F. J. Structural and Electronic Properties of Grain Boundaries in Graphite: Planes of Periodically Distributed Point Defects. *Phys. Rev. B* **2009**, *79*, 195429.
30. Červenka, J.; Katsnelson, M. I.; Flipse, C. F. J. Room-Temperature Ferromagnetism in Graphite Driven by Two-Dimensional Networks of Point Defects. *Nat. Phys.* **2009**, *5*, 840–844.
31. Feenstra, R. M.; Stroscio, J. A.; Fein, A. P. Tunneling Spectroscopy of the Si(111)2 × 1 Surface. *Surf. Sci.* **1987**, *181*, 295–306.
32. Hamers, R. J.; Padowitz, D. F. Methods of Tunneling Spectroscopy with the STM. In *Scanning Probe Microscopy and Spectroscopy: Theory, Techniques, and Applications*; Bonnell, D. A., Ed.; Wiley-VCH: New York, 2001; pp 59–110.
33. Levy, N.; Burke, S. A.; Meaker, K. L.; Panlasigui, M.; Zettl, A.; Guinea, F.; Neto, A. H. C.; Crommie, M. F. Strain-Induced Pseudo-Magnetic Fields Greater than 300 T in Graphene Nanobubbles. *Science* **2010**, *329*, 544–547.
34. Deshpande, A.; Bao, W.; Miao, F.; Lau, C. N.; LeRoy, B. J. Spatially Resolved Spectroscopy of Monolayer Graphene on SiO₂. *Phys. Rev. B* **2009**, *79*, 205411.
35. Zhao, L.; He, R.; Rim, K. T.; Schiros, T.; Kim, K. S.; Zhou, H.; Gutiérrez, C.; Chockalingam, S. P.; Arguello, C. J.; Pálová, L.; et al. Visualizing Individual Nitrogen Dopants in Monolayer Graphene. *Science* **2011**, *333*, 999–1003.
36. Lv, R.; Li, Q.; Botello-Méndez, A. R.; Hayashi, T.; Wang, B.; Berkdemir, A.; Hao, Q.; Elias, A. L.; Cruz-Silva, R.; Gutiérrez, H. R.; et al. Nitrogen-Doped Graphene: Beyond Single Substitution and Enhanced Molecular Sensing. *Sci. Rep.* **2012**, *2*, 586.
37. He, K. T.; Wood, J. D.; Doidge, G. P.; Pop, E.; Lyding, J. W. Scanning Tunneling Microscopy Study and Nanomanipulation of Graphene-Coated Water on Mica. *Nano Lett.* **2012**, *12*, 2665–2672.
38. Zhang, Y.; Brar, V. W.; Girit, C.; Zettl, A.; Crommie, M. F. Origin of Spatial Charge Inhomogeneity in Graphene. *Nat. Phys.* **2009**, *5*, 722–726.
39. Xue, J.; Sanchez-Yamagishi, J.; Bulmash, D.; Jacquod, P.; Deshpande, A.; Watanabe, K.; Taniguchi, T.; Jarillo-Herrero, P.; LeRoy, B. J. Scanning Tunnelling Microscopy and Spectroscopy of Ultra-flat Graphene on Hexagonal Boron Nitride. *Nat. Mater.* **2011**, *10*, 282–285.
40. Rutter, G. M.; Crain, J. N.; Guisinger, N. P.; Li, T.; First, P. N.; Stroscio, J. A. Scattering and Interference in Epitaxial Graphene. *Science* **2007**, *317*, 219–222.
41. Yang, H.; Mayne, A. J.; Boucherit, M.; Comtet, G.; Dujardin, G.; Kuk, Y. Quantum Interference Channelling at Graphene Edges. *Nano Lett.* **2010**, *10*, 943–947.
42. Tian, J.; Cao, H.; Wu, W.; Yu, Q.; Chen, Y. P. Direct Imaging of Graphene Edges: Atomic Structure and Electronic Scattering. *Nano Lett.* **2011**, *11*, 3663–3668.
43. Hasegawa, Y.; Avouris, P. Direct Observation of Standing Wave Formation at Surface Steps Using Scanning Tunneling Spectroscopy. *Phys. Rev. Lett.* **1993**, *71*, 1071–1074.
44. Shallcross, S.; Sharma, S.; Kandelaki, E.; Pankratov, O. A. Electronic Structure of Turbostratic Graphene. *Phys. Rev. B* **2010**, *81*, 165105.
45. Hass, J.; Varchon, F.; Millán-Otoya, J. E.; Sprinkle, M.; Sharma, N.; de Heer, W. A.; Berger, C.; First, P. N.; Magaud, L.; Conrad, E. H. Why Multilayer Graphene on 4H-SiC(0001) Behaves Like a Single Sheet of Graphene. *Phys. Rev. Lett.* **2008**, *100*, 125504.
46. Sprinkle, M.; Hicks, J.; Taleb-Ibrahimi, A.; Le Fèvre, P.; Bertran, F.; Tinkey, H.; Clark, M. C.; Soukiasian, P.; Martinotti, D.; Hass, J.; et al. Multilayer Epitaxial Graphene

Grown on the SiC Surface; Structure and Electronic Properties. *J. Phys. D: Appl. Phys.* **2010**, *43*, 374006.

47. Luican, A.; Li, G.; Reina, A.; Kong, J.; Nair, R. R.; Novoselov, K. S.; Geim, A. K.; Andrei, E. Y. Single-Layer Behavior and Its Breakdown in Twisted Graphene Layers. *Phys. Rev. Lett.* **2011**, *106*, 126802.

48. Salehi-Khojin, A.; Estrada, D.; Lin, K. Y.; Bae, M.; Xiong, F.; Pop, E.; Masel, R. I. Polycrystalline Graphene Ribbons as Chemiresistors. *Adv. Mater.* **2012**, *24*, 53–57.

49. Stander, N.; Huard, B.; Goldhaber-Gordon, D. Evidence for Klein Tunneling in Graphene p-n Junctions. *Phys. Rev. Lett.* **2009**, *102*, 026807.

50. Young, A. F.; Kim, P. Quantum Interference and Klein Tunnelling in Graphene Heterojunctions. *Nat. Phys.* **2009**, *5*, 222–226.

51. Katsnelson, M. I.; Novoselov, K. S.; Geim, A. K. Chiral Tunnelling and the Klein Paradox in Graphene. *Nat. Phys.* **2006**, *2*, 620–625.

52. Cheianov, V. V.; Fal'ko, V.; Altshuler, B. L. The Focusing of Electron Flow and a Veselago Lens in Graphene p-n Junctions. *Science* **2007**, *315*, 1252–1255.

53. Koepke, J. C.; Wood, J. D.; Estrada, D.; Ong, Z.-Y.; Xiong, F.; Pop, E.; Lyding, J. W. Atomic-Scale Study of Scattering and Electronic Properties of CVD Graphene Grain Boundaries. *Proceedings of the IEEE Conference on Nanotechnology* 2012, Birmingham, UK, 20–23 Aug. **2012**, pp. 1–4. DOI: 10.1109/NANO.2012.6322107.

54. Brockenbrough, R. T.; Lyding, J. W. Inertial Tip Translator for a Scanning Tunneling Microscope. *Rev. Sci. Instrum.* **1993**, *64*, 2225–2228.

55. Ferry, D. K. Short-Range Potential Scattering and Its Effect on Graphene Mobility. Submitted for publication.